Title

Spectral tracing of deuterium for imaging glucose metabolism

Journal

Nature Biomedical Engineering, 3(5)

ISSN

2157-846X

Authors

Zhang, Luyuan
Shi, Lingyan
Shen, Yihui
et al.

Publication Date

2019-05-01

DOI

10.1038/s41551-019-0393-4

Peer reviewed

HHS Public Access

Author manuscript

Nat Biomed Eng. Author manuscript; available in PMC 2019 October 29.

Published in final edited form as:

Nat Biomed Eng. 2019 May ; 3(5): 402–413. doi:10.1038/s41551-019-0393-4.

Spectral tracing of deuterium for imaging glucose metabolism

Luyuan Zhang[1,&], **Lingyan Shi**[1,&], **Yihui Shen**[1,&], **Yupeng Miao**[1], **Mian Wei**[1], **Naixin Qian**[1], **Yinong Liu**[1], and **Wei Min**[1,2,*]

[1]Department of Chemistry, Columbia University, New York, NY 10027, USA

[2]Kavli Institute for Brain Science, Columbia University, New York, NY 10027, USA

Abstract

Cells and tissues often display pronounced spatial and dynamical metabolic heterogeneity. Prevalent glucose-imaging techniques report glucose uptake or catabolism activity, yet do not trace the functional utilization of glucose-derived anabolic products. Here, we report a microscopy technique for the optical imaging, via the spectral tracing of deuterium (referred to as STRIDE), of diverse macromolecules derived from glucose. Based on stimulated-Raman-scattering imaging, STRIDE visualizes the metabolic dynamics of newly synthesized macromolecules, such as DNA, protein, lipids and glycogen, via the enrichment and distinct spectra of carbon–deuterium bonds transferred from the deuterated glucose precursor. STRIDE can also use spectral differences derived from different glucose isotopologues to visualize temporally separated glucose populations in a pulse–chase manner. We also show that STRIDE can be used to image glucose metabolism in many mouse tissues, including tumours, the brain, the intestine and the liver, at a detection limit of 10 mM of carbon–deuterium bonds. STRIDE provides a high-resolution and chemically informative assessment of glucose anabolic utilization.

Glucose is arguably the most essential nutrient for animals. It supplies central metabolism, and thus it is of pivotal importance for the sustenance of cellular homeostasis and growth. Glucose metabolism can be regulated by various cell-dependent and tissue-dependent factors, such as energy expenditure, biosynthesis demand, and nutrient accessibility [1–3]. Hence, metabolic heterogeneity is prominent across different length scales, such as in hierarchically organized tissues[4,5] and metabolically reprogrammed tumors[2]. Consequently, a number of powerful glucose-imaging tools have been developed for fundamental studies as well as for diagnostics. Positron emission tomography reports glucose uptake activity using [^{18}F]-FDG, a non-metabolizable glucose analogue[6]. Nuclear magnetic resonance (NMR)-

*Corresponding author, wm2256@columbia.edu.

&These authors contributed equally

Author contributions

L. Z., L. S., Y.S. and W.M. designed the experiment. L. Z. and L. S. performed mice labelling and imaging. L. Z., M. W., Y. L. and L. S. performed macromolecule isolation and analysis. Y. M. and N. Q. performed NMR measurement and analysis. L. Z., L. S., Y.S. and Y. M. analyzed the data. Y. S., L.Z. and W.M. wrote the manuscript with the contributions from all authors.

Competing interests

The authors declare no competing interests.

based imaging measures glucose accumulation via saturation transfer from hydroxyl proton to water[7]. ^{13}C3-NMR spectroscopic imaging resolves soluble glycolytic products via hyperpolarized [^{13}C]-glucose[8]. Imaging mass spectrometry with isotope-labeled glucose provides chemical analysis of metabolites or their ion fragments desorbed from the sample with certain mass coverage[9,10]. Optical imaging can provide an in-situ approach with high resolution. In particular, fluorescence or Raman imaging can report glucose uptake activity using non-metabolizable glucose analogs[11,12].

It is important to note that glucose metabolism consists of multifaceted processes spanning from catabolism to anabolism and to macromolecule synthesis[13]. Specifically, after being taken up into the cell, glucose catabolism breaks down carbon chains for the supply of energy, meanwhile providing substrate for biosynthesis of a variety of precursors including nucleotides, amino acids and fatty acids. These anabolic products further feed cell renewal and proliferation by building biological macromolecules. Excess glucose can also be stored as polymers (e.g. glycogen in animals). It has been increasingly recognized that the diverging allocation of glucose towards synthesis of various macromolecules (such as nucleic acids, glycogen, protein and lipids) is important manifestation of cells' functional status. Notable examples include reprogramming of glucose metabolism dedicated to biomass production for tumor cell proliferation[14,15], and the intricate crosstalk of metabolic regulation between glucose and lipid in liver[16,17]. However, the existing glucose imaging tools mentioned above (such as PET, NMR, and fluorescence) are mostly designed for visualizing the earlier processes of glucose metabolism including uptake or flux into small molecule metabolites. Unfortunately, the later utilization of glucose anabolic products towards macromolecule synthesis remains largely inaccessible to these imaging techniques. Hence, a technical advance along this line should not only provide the full picture of glucose metabolism but also convey valuable information about functional status of cell, tissues and organs.

Raman spectroscopy characterizes molecular vibration by their inelastic photon scattering, and thus informs the concentration and composition of chemical bonds inside a specimen. Different types of molecules can be identified based on their signature chemical moieties, such as CH_2 for lipid and amide or CH_3 for protein. However, Raman (micro)spectroscopy relies on the weak spontaneous scattering, thus is not ideal for high-speed imaging. The detection and sensitivity and imaging speed are greatly improved in stimulated Raman scattering (SRS) microscopy[18–21]. As a nonlinear optical technique, SRS utilizes two synchronized pulsed lasers (normally in the near infrared or visible range), which create a beating field at their difference frequency to selectively accelerate the matching molecular vibrational transition by up to 10^8 times. The resulting intensity change of the incident beams (denoted as stimulated Raman loss or gain) after light-molecule interaction is proportional to the analyte concentration, while the quadratic laser power dependence enables 3-dimensional optical sectioning. SRS fully preserves the spectra of spontaneous Raman scattering, thus a stack of hyperspectral images (at selected frequencies) can be obtained by tuning the laser wavelength. In this manner, non-vibrational-resonance background can be subtracted by acquiring image at off-peak frequency. The spatial resolution and tissue penetration are similar to that of two-photon fluorescence microscopy, suitable for high-resolution imaging of animal tissues.

Towards this unmet goal of mapping glucose metabolism, herein we develop Spectral TRacing of DEuterium isotope (STRIDE) microscopy towards high-spatial-resolution mapping of glucose-derived macromolecule synthesis activity based on Raman spectroscopy and SRS imaging. We administered deuterium-labeled glucose ([D]-glucose) to cells or mouse, and tracked the enrichment of carbon-deuterium (C-D) bonds in macromolecules with multichannel SRS microscopy. C-D bonds produce distinct Raman peaks in "cell-silent" window without interference from endogenous molecules, which reports metabolic activity[21–23]. For chemical specificity, we discovered previously unknown C-D Raman spectral signatures that distinguish various types of glucose-derived macromolecules, which we attributed to different chemical environment experienced by the C-D bond in the macromolecules. Such principle of STRIDE, together with a linear unmixing algorithm we developed, allows visualization and interpretation of how glucose is allocated to diverging biosynthesis pathways among protein, lipid, nucleic acids, and glycogen. We coupled STRIDE with multi-channel SRS imaging to dissect multiplex biosynthesis pathways of macromolecules *in vivo*. In cases where C-D bond enrichment was detectable by SRS (10mM C-D bonds), we obtained tissue metabolic histology, through which we identified markedly high lipid synthesis activity in specific brain regions during developmental period and surprisingly efficient lipid absorbing ability of the neonatal intestinal epithelium. Moreover, glucose utilization in tumor xenografts was assessed. Furthermore, we developed a two-color pulse-chase technique by employing spectral fingerprinting derived from different glucose isotopologues and demonstrated visualizing biosynthetic activity in different time windows.

[D_7]-glucose is a metabolic probe of macromolecule synthesis in cells and mice

We first validated that [D_7]-glucose, a glucose isotopologue with deuterium labeling on all its carbons, can be used as a metabolic probe of macromolecule synthesis for SRS microscopy. Raman spectra obtained from cells cultured in [D_7]-glucose-substituted medium revealed a band around 2150 cm^{-1} in the cell-silent region (1800~2600 cm^{-1}), confirming the formation of C-D bonds in cells (Fig. 1a). We then acquired SRS images targeting at this frequency, the intensity of which is proportional to the concentration of C-D bonds and shows increment up to 3 days (Fig. 1b). This rate is much slower than the reported glucose uptake rate (reaching steady state in an hour)[12], thereby reflecting long-term accumulation of C-D bonds derived from [D_7]-glucose. In fact, signal from transported [D_7]-glucose can hardly be detected at out detection limit (~4 mM) (Fig. 1b, Fig. S1a). Moreover, unlike an earlier developed glucose uptake reporter[12], the accumulated C-D signal is not affected by permeating cell membrane via fixation (in which case the small-molecule metabolites from glucose would have been depleted) (Fig. S1b), yet was reduced by the inhibition of fatty acid synthesis (Fig. S1c). Together, these measurements confirmed that the observed signal originated from newly accumulated macromolecules rather than small-molecule metabolites from [D_7]-glucose.

Compared to labeling *in vitro* cell cultures as demonstrated previously[24–26], it is much harder to predict glucose utilization in whole animal *in vivo* with the presence of many other

nutrient sources. Towards this challenging goal, we explored different *in vivo* administration approaches. We found administration of up to 10% [D_7]-glucose in drinking water to be a convenient non-invasive approach for metabolic labeling in mice [27]. After 10 days of labeling, post-mortem tissue slices were obtained for SRS imaging through laser scanning (Fig. 1c). At the same frequency (2150 cm^{-1}), C-D bond accumulation was successfully visualized in tissues such as stomach and fat pad, indicating broad appearance of metabolic activity (Fig. 1d). Non-resonance background was measured at 1900cm^{-1} by tuning the laser, and then subtracted from the on-resonance image (2150cm^{-1}). Using [D_7]-glucose or unlabeled glucose or their equal mixture, we are able to vary the deuterium fraction without changing the total glucose amount in drinking water. In such three conditions, average tissue SRS signal at 2150cm^{-1} are roughly proportional to the [D-glucose] percentage in drinking water, demonstrating highly specific and quantitative detection of C-D bonds by SRS imaging (Fig. 1e). It is worth noting that the labeling and imaging procedure is for general application, which can certainly be optimized for specific cases. For example, the concentration of [D_7]-glucose can be lowered to 2% while still generating satisfying signal in fat pad (Fig. S1d). In addition, live imaging can be performed in principle, leveraging the optical sectioning, good tissue penetration and *in vivo* compatibility of SRS microscopy[21]. Here we demonstrated live imaging of the mouse ear at a frame rate of 1.6 sec per frame, from which flow of blood cell is evident in both on-resonance (2150 cm^{-1}) and off-resonance (1900 cm^{-1}) images (supplementary video, Fig. 1f).

Principle of STRIDE

Images acquired at single frequency (2150 cm^{-1}) map the overall accumulation of glucose-derived C-D bonds. Yet as a universal carbon source, glucose should supply synthesis of diverse biomass including glycogen, nucleic acids, lipids, and proteins. Such divergence is reflected in atom tracing of deuterium along the central metabolic pathways, showing [D] labeling in various metabolic precursors[13] (Fig. 2a). Hence, C-D SRS signal should represent mixed contribution from these macromolecules. Indeed, though methanol removed all the lipids (confirmed by SRS imaging targeting carbon-hydrogen bonds, which showed almost diminished signal in lipid image but no change in protein image), it cannot remove all the C-D signal in cells (Fig. 2b). How the supplied glucose is allocated for different macromolecule synthesis? The ability to address this question would not only provide the full picture of glucose metabolism but also convey valuable information about functional status of cells, tissues and organs.

To distinguish the different macromoleculs derived from [D_7]-glucose, we sought to identify underlying C-D Raman spectral signatures that are sensitive to chemical environment. Like NMR spectroscopy where nuclei can be distinguished by their local chemical environment [7,14], vibrational frequency in Raman spectra also reflects the local chemical environment of the bond, such as polarity. We postulated that the chemically diverse macromolecules might create different C-D vibrational spectra. To test this, we first labeled cultured HeLa cells with [D_7]-glucose, from which we isolated lipids, proteins and nucleic acids. We then acquired and studied their Raman spectra. We also obtained Raman spectra from glycogen acutely accumulated in [D_7]-glucose-labeled mouse liver (verified by perchloric acid dissolvability, Fig. S2, a-c). Notably, though spanning almost the same frequency range, C-D

Raman spectra from the above four types of molecules exhibited remarkably different peak position and shape from each other and from [D_7]-glucose solution (Fig. 2c) (peak frequency summarized in Supplementary Table 1). Glycogen and nucleic acid, made from glucose and (deoxy)ribose, show multi-peak spectral feature (2124, 2170, 2234 cm^{-1}) (Fig. 2c), corresponding to preservation of more C-D bonds as well as their distinct chemical environment attached to the sugar rings[28] (Fig. 2b). On the contrary, protein and lipid, made from amino acids and fatty acids, respectively, show only one major peak (Fig. 2c). This agrees with more loss of [D] going through glycolysis and tricarboxylic acid cycle (Fig. 2b). To confirm this spectral finding, we compared to the reference spectra of [D]-labeled fatty acid and amino acids (Fig. S2, d-f) (Supplementary Table 1). We found good agreement between the peak frequency between our lipid extract (2142 cm^{-1}) and singly labeled C-D in deuterated fatty acid (2142 cm^{-1}), which is in nonpolar aliphatic chemical environment. Similarly, the peak frequency of our protein extract (2192 cm^{-1}) matches that from singly labeled C-D in deuterated amino acids (2192 cm^{-1}), which is in more polar chemical environment. Altogether, Raman spectral features reflect the distinct chemical environment experienced by C-D bond in the specific biomacromolecule.

To further ensure the Raman spectrum of each macromolecule discovered above is reproducible and accurate, we obtained *in situ* lipid and protein Raman spectra from [D_7]-glucose labeled cells and mouse tissues through measuring signal that is susceptible and resistant to methanol wash, respectively (Fig. S2, g-j), and also the Raman spectra from [D_7]-glucose labeled tissue extracts (Fig. S2, k-l). All these spectra agree well. To improve accuracy, we then used the average of these spectra as our *a priori* standards to guide linear unmixing. We call such spectra-guided metabolic tracing technique as Spectral TRacIng of DEuterium isotope (STRIDE).

Multiplexed imaging and quantification of macromolecule synthesis activity using STRIDE

Next, we integrated STRIDE with multi-channel SRS imaging. For *n* species with distinguishable spectra, linear unmixing can be performed with intensities at as few as *n* different frequencies (i.e. channels). Therefore, we took SRS images at several selected frequencies by tuning the laser wavelength, and used the coefficients developed from the normalized standard spectra to calculate the unmixed images (Fig. 3). Here we leveraged the linear intensity-concentration dependence of SRS and the faithful correspondence of SRS intensity to that of Raman spectra[19]. We applied multi-channel imaging and unmixing to HeLa cells cultured with [D_7]-glucose, where signal from *de novo* lipid synthesis (CD_L), protein synthesis (CD_P), and DNA replication (CD_D) are comparable to each other and can be successfully separated (Fig. 3, a-c). Glycogen signal can be omitted in such non-specialized cell culture. DNA synthesis was detectable in mitotic cells with condensed chromosome but not in non-mitotic cells due to the volume dilution (factor of 5, see Supplementary text) (Fig. S3a). It is then reasonable to omit DNA signal in non-mitotic cells for the rest of this study. We also applied this technique to the liver of mouse fed with [D_7]-glucose for 10 days and then acutely stimulated and labeled for 8h after overnight fasting. With such labeling, signal from acute glycogen synthesis (CD_G) is comparable to those from

long-term accumulated protein (CD_P) and lipid signals (CD_L), and can be successfully separated (Fig. 3, d-f). Distinct spatial patterns can be found in these channels. For example, CD_L signal reveals accumulation of lipid metabolites in LDs, while CD_G reveals glycogen accumulation in cytoplasm, which shows halo pattern around nucleus.

In addition to spatial information, quantitative information can be obtained by at least three means as following. Firstly, absolute SRS intensity can be used to compare metabolic activity under different conditions. As an example, we found that 16-hr pre-starvation increased liver glycogen signal (Fig. S3b). In a second quantification approach, ratio between two macromolecule channels, such as CD_P and CD_L, can be used to indicate differential utilization of glucose metabolism. For example, we generated CD_P/CD_L ratio images for a variety of tissues, including heart, pancreas, kidney, duodenum, stomach, and fat pad, thereby generating a tissue atlas of macromolecule-specific glucose metabolism (Fig. 4a). These ratio images captured highly-specialized organs, such as cardiac muscle (high protein synthesis) and fat tissue (lipid synthesis), which is consistent with their metabolic function. Interestingly, metabolic heterogeneity can be observed at subcellular scale. For tissues along the gastrointestinal tract, the highest ratio (or protein-dominating) is generally found in nucleus, while the supportive tissue or duct has the lowest ratio (or lipid-dominating).

The third way of quantitative interpretation is through the ratio of C-D and C-H channel. SRS images targeting at the frequency of C-H (lipid, CH_L; protein, CH_P) map the concentration of unlabeled C-H bonds in lipid or protein[29]. Thus, intensity ratio between corresponding C-D and C-H channels reflects the renewal or turnover of the specific biomolecule. As an example, we tracked the skin sebaceous gland of mouse drinking 5% [D_7]-glucose water each day from day 1 to day 6. The lipid production and secretion in sebaceous gland are known to follow holocrine mechanism, in which peripheral sebocytes rupture themselves and release the contents in the central duct[30]. By calculating the CD_L/CH_L ratio image, we found that glucose-supplied lipid renewal actually first appeared on the periphery of gland and then gradually migrated to the center thereafter (Fig. 4b), offering a new insight to the metabolism aspect of holocrine secretion process. Moreover, with sufficient spatial resolution, remnants of sebocytes with much lower metabolic turnover could readily be found in the duct (e.g. day 6).

This third quantification method using CD/CH ratio also offers a checkpoint to be cross-referenced with proton-NMR spectroscopy. Herein we obtained hydrogen (H-) and deuterium (D-) NMR spectra of tissue lipid extracts and quantified the ratio D/H (Fig. S4a). We also calculated the CD/CH ratio for both Raman spectra (using peak intensity) and SRS imaging (using area-averaged intensity). The ratios show good correspondence among the three different measurements (Fig. S4b), validating the quantitative reliability of STRIDE.

STRIDE imaging of metabolic activity during development and tumor

Employing the three quantification methods introduced above, STRIDE imaging can be applied to study metabolic dynamics during the developmental period and tumor progression. We thus labeled a young mouse labeled during the developmental period (E11

to P21) through administering [D_7]-glucose in the drinking water (2%) to its mother, and obtained its tissue atlas of macromolecule synthesis. Brain is of special interest during development. We thus compared the brain of young mouse (labeled during E11-P21) with adult mouse labeled for the same concentration and time. The whole brain tissue mapping, as in SRS intensity, readily reveals faster basal-level lipid and protein metabolism in young mouse brain compared to the adult brain (Fig. 5a). Quantitative comparison of the absolute SRS image intensity revealed highly active lipid synthesis from young brain than adult brain in multiple regions including caudoputamen (CP), fimbria (FI), optic tract (OPT), lateral habenula (LH), lateral hypothalamic area (HY), mammilothalmic tract (MTT), hippocampus (HPF), stria terminalis (ST), and corpus callosum (CC) in cerebrum (Fig. 5b, Fig. S5, a-b).

Comparing lipid signal between the CD and CH channels reveals a large age difference in lipid turnover, especially in the white matter of cerebellum (Fig. 5c). Intensity profiles across the cerebellum layers show active lipid turnover in the young brain but almost no turnover in the adult brain (Fig. 5d). Remarkably, the pattern in young brain are spatially correlated with the expression profiles of myelin basic protein (Fig. S5, c-f), a major constituent of myelin sheath[31], and temporally coincides with the restricted myelination window during development[32]. Thus, our observation supports previous findings that myelination requires tremendous effort in lipid synthesis in the developmental period[33]. Besides brain, we also obtained other tissues from the young mouse, including pancreas, heart, muscle, lung, kidney, stomach and fat pad, constituting the tissue atlas of metabolic activity (Fig. S5g). Interestingly, a clearly higher protein synthesis activity was observed in brown adipose (marked by its smaller lipid droplet size) compared to white adipose, indicating more diverse utilization of glucose possibly to fulfill the various secretion roles of brown adipose[34] (Fig. S5g).

A hallmark of tumor metabolism is the significant upregulation of glucose metabolism[3,15]. We thus applied STRIDE imaging to assess macromolecule synthesis in xenograft tumor mouse models. We administered [D_7]-glucose drinking water to mice during 30–40 day post injection of U87MG brain glioblastoma xenograft[35]. After harvesting brain tissue slices containing the solid tumor (Fig. S5h), we identified the tumor regions based on the position of implantation as well as hypercellularity according to label-free SRS histology[29,35] (Fig. S5i). As expected, compared to the normal brain tissue across the boundary, both lipid or protein synthesis are more active in tumor according to the ratio images of CD_L/CH_L and CD_P/CH_P (Fig. S5j). Yet, the utilization of glucose is also different in tumor according to CD_P/CD_L image, showing more favored protein synthesis from glucose.

STRIDE imaging reveals fast and unidirectional lipid absorption in newborn mouse intestine

In the small intestine of the young mouse (labeled E11-P21) but not the adult mouse, we observed surprisingly large signal in globule structures with diameter up to 3μm (Fig. 6a). As this is likely a steady-state result after long term labeling, the true spatial temporal dynamics remain hidden. We then shortened the administration of [D_7]-glucose drinking water to 5 hours for the lactating mother, and then restrict breast milk feeding of the pup

within only 15 minutes. Early radioisotope measurement on suckling rodents hinted on about half an hour time lag between nutrient supplementation and intestinal absorption but could not confirm due to poor detectability at early time points[36]. Surprisingly, even within such a short interval of 15 minutes, we observed bright C-D signal in the villi of small intestine of the pup (Fig. 6b, see quantification in Supplementary Table 3), indicating high efficiency of nutrient absorption and processing by neonatal intestinal epithelium. These globule structures are dominated by signal in CD_L channel and can be stained by Nile Red for neutral lipid (Fig. 6b), suggesting they are intracellular lipid droplets (LDs) or assembled chylomicrons. Indeed, it is known that fat makes up nearly half of the milk dry mass and that milk fat is the major nutrient for the suckling pup[37,38].

We then captured spatially unidirectional fat synthesis and repackaging in neonatal mouse intestine. Nutrient absorption across intestinal epithelium is primarily carried out by enterocytes[39]. These highly polarized cells take up nutrients at their brush boarder surface and transported them across the basal membrane where the nutrients enter circulation system lying in the center of the villi. Leveraging the optical sectioning ability of SRS, we obtained depth-resolved images from brush boarder surface deep into the villi (Fig. 6, c-d), and clearly revealed depth dependence of droplet size (Fig. 6e). Going from apical surface where absorption of milk fats takes place, through the cytoplasm of enterocyte, to the capillary and lacteal network beneath which chylomicrons are secreted, the diameter of the largest droplet increases from 1.6μm to 2.9μm, indicating a unidirectional fat synthesis and repackaging from apical surface to basal membrane of the enterocytes. Altogether, STRIDE microscopy provides high spatiotemporal resolution to directly visualize maternal nutrient transfer, and reveals the highly efficient and unidirectional process of fat absorption and processing by the neonatal intestinal epithelium.

STRIDE imaging of glucose isotopologues for temporally resolved metabolic dynamics

Pulse-chase analysis is a classic approach to dissect the temporal progression of biological processes. The versatility of probes has enabled pulse-chase assessment in complex settings by labeling different time intervals with probes with distinct colors[40–42]. We next sought to explore whether STRIDE can be developed into a pulse-chase labeling with orthogonal glucose probes, realizing that there exist many partially labeled glucose isotopologues beyond the fully deuterated [D_7]-glucose described above. We noticed the diverging fates and environment of the seven [D]'s in [D_7]-glucose during deuterium atom tracing (Fig. 2a), which underlies the rationale of mass spectrometric analysis that adopts various partially [D]-labeled glucose isotopologues to highlight specific metabolic pathways[43,44]. Inspired by this strategy and realizing the sensitivity of STRIDE to [D] labeling pattern and final chemical environment, we speculated that Raman spectra of macromolecule metabolites may also encode the origin of glucose isotopologue.

We first began with glycogen, which retains most deuterium from glucose. We obtained Raman spectrum of liver glycogen derived from [6,6-D_2]-glucose ([D_2]-glucose thereafter), which indeed showed pronounced difference compared to that from [D_7]-glucose (Fig. 7a,

S6a). We then obtained Raman spectra of lipids and proteins extracted from HeLa cells cultured in [D_7]-glucose, or [D_2]-glucose, or [1-D_1]-glucose (normalized at 1450cm^{-1} for lipid, and 1670cm^{-1} for protein). The spectra derived from each glucose isotopologue showed apparent difference not only in overall intensity but also the relative intensities at multiple frequencies (Fig. 7, b-c). More insights of pathway-specific contribution can be gained by analyzing the intensity and assigning peak frequencies in these spectra (See Supplementary text). Therefore, based on the clearly distinguishable spectra of macromolecules derived from [D_7]-glucose and [D_2]-glucose, we chose these two isotopologues as orthogonal probes to label temporally separated populations within the same sample.

As a proof-of-concept demonstration of pulse-chase labeling and imaging, we sequentially administered [D_7]-glucose and [D_2]-glucose (each for 24 hrs) in the drinking water of a mouse and obtained the skin tissue, where glucose is almost exclusively used for lipid synthesis in sebaceous gland. After linear unmixing based on the lipid spectra derived from the two isotopologues (Fig. S6b), we successfully visualized de novo lipid synthesis in these two successive time windows. Spatial segregation of lipids synthesized earlier and later in time was evident in sebaceous gland (Fig. 7d): compared to the later pool, the earlier pool has migrated closer to the secreting duct in the center, which is consistent with the gradient observed earlier (Fig. 4b).

Similarly, pulse-chase labeling can be used to assess glycogen accumulation in liver. The mouse liver is divided into basic functional units termed lobules, inside which a general nutrient gradient can be observed from portal vein to central vein. Liver metabolic functions are found to be zonated across the gradient, which is increasingly appreciated for understanding liver architecture[5]. We sequentially administered [D_2]-glucose and [D_7]-glucose (each for 8 hrs) in the drinking water of a mouse fasted overnight. The acute labeling scheme highlights glycogen synthesis in liver without interference from basal level synthesis of other metabolites (Fig. S6c). Applying spectral unmixing, we successfully separated signal of glycogen synthesis derived from the two glucose isotopologues (Fig. S6, d-f). Interesting spatial patterns were observed (Fig. 7e). In general, the later applied label (red) appears throughout the liver lobule, whereas the earlier applied label (green) accumulates more in the pericentral zone and gets depleted around the portal vein. Such a pattern lends support to the faster glycogen turnover in periportal zone reported earlier[45]. Compared to traditional methods of glycogen staining[45] or isolating zonated cells[46], the pulse-chase approach reveals explicit spatial distribution of glycogen synthesized during different time windows within the same liver tissue, avoiding the complication of pre-existing pools or cross-sample variation. The spatial information offered in situ also better reflects zonation in large-scale tissue organization. Metabolic heterogeneity among single cells is also evident from the scattered distribution of cells actively accumulating glycogen (Fig. 7e). With the unmatched spatial resolution for revealing single-cell heterogeneity, STRIDE promises future metabolic phenotyping in the era of single cell omics.

Discussion

We have discovered distinct Raman spectral fingerprints for C-D bonds in macromolecules derived from [D]-labeled glucose, and harnessed it for macromolecule-type-specific metabolic mapping with high spatial resolution. We further exploited C-D Raman spectral fingerprints for spectrally separating [D]-labeled macromolecule from different origins of glucose isotopologues, which enabled two-color pulse-chase probing in different temporal windows and revealed interesting metabolic gradient in sebaceous gland and liver. In this current demonstration we mostly focused on macromolecule type-specific imaging. Although the chemical information may be limited compared to other metabolic tracing and imaging techniques like NMR or mass spectrometry, STRIDE offers a high spatial resolution in a nondestructive way to meet the growing demand of mapping tissue metabolic heterogeneity, thereby complementing the current toolset for assessing metabolic dynamics in animals.

The C-D bond has been increasingly adopted by Raman microscopy as a vibrational tag for imaging metabolic incorporation of precursor molecules [21, 23]. Usually, the C-D bonds in the final biomaterial are detected at the same frequency as in the precursor molecule. In other words, one precursor molecule corresponds to one detection channel, thus monitoring one-type of metabolism at a time. This one-to-one correspondence could be extended to multiple probes [26, 42, 47],while in most cases is still limited to single type of metabolism as a targeted imaging approach. Conceptually, STRIDE of glucose metabolism is different than previously reported deuterium-labeled metabolic precursors. It is based on the central metabolic role of glucose, and extends the chemical information derived from a single probe to the multiplexed imaging of glucose metabolites. This is realized by acknowledging the diverse chemical environment in macromolecules. In other words, in STRIDE, the C-D bond is not only a concentration probe for overall metabolic activity, but also a local sensor for macromolecule identity. This conceptual feature also distinguishes STRIDE from earlier attempts of single-channel glucose metabolic imaging (mostly reporting lipid synthesis) in bacteria or cultured cells.[24, 25, 48-50]

STRIDE imaging can have broad applications, ranging from general assessment of glucose anabolic utilization to visualization of metabolic activity of specialized organs like adipose, pancreas or liver. Depending on the specific applications, the concentration and duration of [D]-glucose administration can be further optimized. In this general demonstration, we administered glucose in drinking water in the concentration range of 2–10% to reveal tissues with low metabolic activity. We realize that glucose, as a nutrient source itself, might potentially alter metabolism systematically. We thus measured the food and water intake, body weight gain, and glucose tolerance in mice with or without drinking 10% glucose for 10 days (Supplementary Table 2). Though long-term administration of glucose reduces food intake, no significant perturbation to glucose tolerance was observed. Moreover, the concentration and/or labeling duration can be effectively reduced if a particular process is of interest. The detection limit is set by two factors: deuterium label incorporation and detection sensitivity of SRS. Only limited number of deuterium finally incorporate into biomass, while most are lost during glycolysis and energy production. At least 10mM C-D bond, corresponding to 0.1–1% deuterium enrichment in macromolecules, is required for

SRS imaging at high spatial resolution. Quantitatively, we have summarized the detected SNR (for 100us pixel dwell time) in some specialized tissues and the corresponding labeling condition (Supplementary Table 3). For example, adipose obtained from mouse drinking 10% glucose for 10 days exhibit SNR = 570 ± 90; liver glycogen obtained from acutely treated mouse (10%, 8h) exhibits SNR = 44 ± 24. Based on the above quantification, there is arguably room for parameter optimization when special considerations should be taken.

Although most images were acquired from tissue slices in transmission mode, the labeling and optical detection are non-invasive, allowing the imaging of a live mouse (Fig. 1e and Supplementary video). The current imaging depth is comparable to that of typical two-photon fluorescence microscopy (hundreds of micrometres); thus, for imaging internal organs, post-mortem tissue sectioning is still required. We envision the applicability of this technique *in vivo* with instrumentation upgrade to epi-detected SRS and to the recently developed coherent Raman scattering endoscope [51, 52].

Methods

Materials.

Metabolic labeling was achieved with [D_7]-glucose, [6,6-D_2]-glucose (Cambridge Isotope Inc.) and [1-D_1]-glucose (Sigma-Aldrich). Spectra were assigned using standards including fatty acids, [12-D_1]-palmitic acid (Cambridge Isotope Inc., dissolved in DMSO), [U-D_{31}]-palmitic acid (Sigma-Aldrich, dissolved in DMSO); amino acids, [2,3,3,3-D_4]-alanine, [D_8]-valine (Cambridge Isotope Inc. dissolved in PBS); and [U-D_8]-glycerol (Cambridge Isotope Inc.). 3-OPG used to measure glucose uptake was reported earlier[12]. TVB-3166 (Sigma-Aldrich) was used to inhibit fatty acid synthesis. Perchloric acid (Fisher Scientific) was used to remove glycogen in tissue.

Cell culture, labeling, and imaging.

Cell lines used in this study are PC3 (ATCC), HeLa (ATCC), MCF7 (ATCC), RWPE-1 (ATCC), U87MG (ATCC). Cell cultures were maintained according to ATCC instruction in their designated medium. For labeling cell culture, media were replaced with glucose-free DMEM (ThermoFisher,11966) supplemented with [D_7]-glucose (0.45%, w/v). For DNA labeling, serum is reduced to 5% in culture. For acquiring spectra of isolated macromolecule, serum is reduced to 2% in culture to increase labeling efficiency. For live imaging, cells were plated onto glass-bottom dish (MATTEK); for imaging as fixed, cells were plated onto coverslips (No. 1, FisherBrand). Cells were first cultured in regular medium, and then switched to [D_7]-glucose-substituted medium for designated duration. Upon imaging, cells were either immersed live in PBS or fixed with 4% PFA for 30min, and the coverslip is sandwiched onto a glass slide (1mm thick, VWR) with imaging spacer (0.12mm thick, SecureSeal).

Macromolecule isolation from cultured cell.

Hela cells were first cultured in 25 cm^2 culture flask in complete medium until 50% confluency. The medium was then replaced with DMEM substituted with 0.45% [1-D_1]-glucose, [6,6-D_2]-glucose or [D_7]-glucose and 2% FBS. Fresh medium was replenished

every 2 days. After 6 days, cells were dissociated and harvested, and DNA, RNA and proteins were extracted using TRIzol Reagent (ThermoFisher) according to the manufacturer's manual. For lipid extraction, cells were harvested and suspended in 1 mL PBS, and mixed with 1.3 mL chloroform and 2.7 mL methanol. The solution was centrifuged at 4000 rpm for 5 minutes. The supernatant was transferred to a new clean tube, and mixed with 1 mL 50 mM citric acid (Sigma-Aldrich), 2 mL of distilled water and 1 mL of chloroform. After brief shaking and mixing, the tube was centrifuged at 4000 rpm for 10 minutes. The material separated into three phases: a water/methanol upper phase; a middle phase of precipitated protein; and a lower chloroform phase. Lipids are dissolved in the lower chloroform phase. The chloroform phase was separated, dropped on cover glass and air-dried.

Mouse labeling.

All animal experiments were conducted in adherence to experimental protocol approved by IACUC (AC-AAAQ0496). For normal condition, wild type (strain C57BL/6J, Jackson Laboratory) mice were given drinking water containing [D_7] or [6,6-D_2]-glucose at designed concentration. Mice had free access to regular chow during this time. For overnight fasting, mice were fasted for 18 hours with access to regular drinking water only. For labeling mice in embryonic period or neonatal period, [D_7]-glucose was administered to the pregnant or the lactating wild type female mouse in drink water. For labeling and imaging in skin sebaceous gland, nude mice (strain J:NU, Jackson Laboratory) were used to avoid strong absorption of pigment. The ear skin was either clipped or directly imaged alive.

Mouse tumor xenograft.

Orthotopic brain glioblastoma xenograft was established by intracranial implantation of U87MG human glioma cells. Briefly, nude mice (strain J:NU, Jackson Laboratory) were anesthetized and positioned in stereotaxic instrument (David Kopf Instruments), and then a small section (2 mm in diameter) of the skull was ground with a dental drill (Braintree Scientific INC) until it became soft and translucent. Subsequently, 1.5×10^5 U87MG tumor cells (in 3 μL) were injected into the frontal region of the cerebral cortex over the course of 5 minutes using a 1.5 mm glass capillary. After the implantation, mouse head skin was closed with SILK sutures (Harvard Apparatus).

Tissue slicing.

After treatment and labeling, the mice were anesthetized and sacrificed by cervical dislocation, and then various organs were harvested. All the mouse tissues were post-mortemly fixed with PFA for more than 48 hours after harvesting. Tissues were then embedded in 4% agarose gel (Sigma-Aldrich), and sliced into 100 μm thin slices using a vibratome (Leica). Brain was sliced coronally. Random orientation was used for other tissue. The tissue slices were collected and sealed between glass slide and coverslip.

Tissue processing.

To remove lipid, tissue slices were soaked in pure methanol for 48 hours and then washed with PBS. To remove glycogen, liver tissue slices were incubated in ice-cold 10% perchloric

acid for one hour and then washed with PBS. To extract lipid from adipose tissue, 1 gram of adipose tissues were harvested and smashed, and suspended in 1 mL PBS, and mixed with 2.6 mL chloroform and 5.4 mL methanol. The solution was centrifuged at 4000 rpm for 5 minutes. The supernatant was transferred to a new clean tube, and mixed with 2 mL 50 mM citric acid (Sigma-Aldrich), 4 mL of water and 2 mL of chloroform. After brief shaking and mixing, the tube was centrifuged at 4000 rpm for 10 minutes to phase separate. Lower chloroform phase containing lipids was obtained and solvent was evaporated to obtain tissue lipid extract.

Nuclear magnetic resonance (NMR) measurement.

NMR spectra were recorded on a Bruker 500 (500MHz) or Bruker 400 (400MHz) Fourier Transform (FT) NMR spectrometer. Lipids extracted from the mice adipose tissues was dried and weighted, and dissolved in 600 μL chloroform with additional 2 μL deuterated chloroform (Cambridge Isotope Laboratory) to obtain deuterium NMR spectra. To obtain hydrogen NMR spectra the lipid extract was re-dissolved in 700 μL deuterated chloroform plus 10 μL chloroform. The two spectra were calibrated and normalized according to the chloroform (δ 7.26ppm) for quantitative estimation of the deuterium substituted ratio.

Spontaneous Raman spectroscopy.

Raman spectra were obtained from fixed cells or tissue as previously described [53]. Briefly, samples were placed on an upright confocal Raman microspectrometer (Xplora, Horiba Jobin Yvon) equipped with 532 nm diode laser source and 1800 l/mm grating at room temperature. The excitation power is ~42 mW after passing through a 50X air objective (MPlan N, 0.75 N.A., Olympus), and 60s acquisition time was used to collect Raman spectra of all samples at a single point under identical conditions. For cultured cells, the Raman background of water and cover glass is removed by subtracting the signal at empty space from the signals collected in cells. For tissue with detectable autofluorescence background such as liver, the acquisition spot on the tissue was first photobleached by the laser for several minutes before spectra acquisition.

Stimulated Raman Scattering Microscopy.

Similar to a previously described setup [54], we used an inverted laser-scanning microscope (FV1200, Olympus) optimized for near-IR throughput and a 25X water objective (XLPlanN, 1.05 N.A., MP, Olympus) with high near-IR transmission for SRS imaging. A picoEMERALD system (Applied Physics & Electronics) supplied synchronized pulse pump beam (with tunable 720–990 nm wavelength, 5–6 ps pulse width, and 80-MHz repetition rate) and Stokes (with fixed wavelength at 1064 nm, 6 ps pulse width, and 80 MHz repetition rate). Stokes is modulated at 8MHz by an electronic optic modulator. Transmission of the forward-going pump and Stokes beams after passing through the samples was collected by a high N.A. oil condenser (N.A. = 1.4). A high O.D. bandpass filter (890/220, Chroma) is used to block the Stokes beam completely and to transmit only the pump beam onto a large area Si photodiode for the detection of the stimulated Raman loss signal. The output current from the photodiode is terminated, filtered, and demodulated by a lock-in amplifier (Zurich, HF2LI) at 8 MHz to ensure shot-noise-limited detection sensitivity. The demodulated signal is fed into analog channel of FV1200 software FluoView

4.1a (Olympus) to form image during laser scanning at a rate of 100us per pixel. For multi-channel SRS imaging, the pump wavelength was tuned so that the energy difference between pump and Stokes matched with the vibrational frequency as described below.

$$\lambda_{pump} = 1 / (1 / 1064 + 10^{-7} * \nu)$$

where v is the vibrational frequency in cm^{-1}. CD channels were acquired at frequencies as shown in figure. CH channels were acquired at 2845 cm^{-1} and 2940 cm^{-1} and unmixed according to an earlier report [55]

In vivo imaging of mouse ear skin.

A nude mouse was given 5% [D_7]-glucose in drinking water and regular chow for 8 days before imaging. The mouse was then kept anesthetized with isoflurane while one ear was gently sandwiched between a cover slip and a glass slide, which were then placed onto the imaging stage with a heating pad that kept the body warm during the imaging session. A faster scanning rate (1.6 sec per frame) was used for live imaging.

Nile Red confocal fluorescence.

Small intestine tissue slice was stained with Nile Red (Invitrogen) at 1μM for 1 hour. It was then washed and imaged by confocal fluorescence built in the same microscope as SRS. The excitation wavelength and filter were 488nm and 505–605nm.

Software.

Image was processed and pseudo colored in ImageJ. For SRS images of CD channels, corresponding off resonance images were taken at 1900cm^{-1} and subtracted from the on-resonance images. Stimulated Raman histology was generated according to previously reported procedure [29]. Basically, the protein channel ($I_{2940} - I_{2845}$) was assigned hematoxylin-like blue color, while the lipid channel (I_{2845}) was assigned eosin-like pink color, and the two channels were merged. Droplet size quantification was done in intestine tissue by applying auto local thresholding and analyzing particles to the depth-resolved image stack. Data analysis and visualization were done in GraphPad and Origin.

Reporting summary.

Further information on research design is available in the Nature Research Reporting Summary linked to this article.

Data availability.

The authors declare that all data supporting the results in this study are available within the paper and its Supplementary Information. All raw and processed images generated in this work are available from the corresponding author on reasonable request.

Supplementary Material

Refer to Web version on PubMed Central for supplementary material.

Acknowledgements

We appreciate the suggestions from Dr. F. Hu and Dr. C. Zheng on this manuscript. W.M. acknowledges support from a National Institutes of Health Director's New Innovator Award (1DP2EB016573), NIH R01 (grant EB020892), the Alfred P. Sloan Foundation, the Camille and Henry Dreyfus Foundation, and a Pilot and Feasibility grant from the New York Obesity Nutrition Research Center

References

1. Saltiel AR & Kahn CR Insulin signalling and the regulation of glucose and lipid metabolism. Nature 414, 799–806 (2001). [PubMed: 11742412]
2. Hensley CT et al. Metabolic Heterogeneity in Human Lung Tumors. Cell 164, 681–694 (2016). [PubMed: 26853473]
3. Vander Heiden MG & DeBerardinis RJ Understanding the Intersections between Metabolism and Cancer Biology. Cell 168, 657–669 (2017). [PubMed: 28187287]
4. Pipeleers DG Heterogeneity in pancreatic β-cell population. Diabetes 41, 777–781 (1992). [PubMed: 1612191]
5. Halpern KB et al. Single-cell spatial reconstruction reveals global division of labour in the mammalian liver. Nature 542, 1–5 (2017).
6. Gambhir SS Molecular imaging of cancer with positron emission tomography. Nat Rev Cancer 2, 683–693 (2002). [PubMed: 12209157]
7. Walker-Samuel S et al. In vivo imaging of glucose uptake and metabolism in tumors. Nat. Med 19, 1067–1072 (2013). [PubMed: 23832090]
8. Rodrigues TB et al. Magnetic resonance imaging of tumor glycolysis using hyperpolarized 13C-labeled glucose. Nat. Med 20, 93–97 (2013). [PubMed: 24317119]
9. Sugiura Y et al. Visualization of in vivo metabolic flows reveals accelerated utilization of glucose and lactate in penumbra of ischemic heart. Sci. Rep 6, (2016).
10. Guillermier C, Poczatek JC, Taylor WR & Steinhauser ML Quantitative imaging of deuterated metabolic tracers in biological tissues with nanoscale secondary ion mass spectrometry. International Journal of Mass Spectrometry (2017). doi:10.1016/j.ijms.2017.08.004
11. Zou C, Wang Y & Shen Z 2-NBDG as a fluorescent indicator for direct glucose uptake measurement. J. Biochem. Biophys. Methods 64, 207–215 (2005). [PubMed: 16182371]
12. Hu F et al. Vibrational Imaging of Glucose Uptake Activity in Live Cells and Tissues by Stimulated Raman Scattering. Angew. Chemie - Int. Ed 54, 9821–9825 (2015).
13. Nelson D, and Cox M Lehninger Principles of Biochemistry (W. H. Freeman & Company, 2005)
14. Chen YJ et al. Differential incorporation of glucose into biomass during Warburg metabolism. Biochemistry 53, 4755–4757 (2014). [PubMed: 25010499]
15. Lunt SY & Vander Heiden MG Aerobic Glycolysis: Meeting the Metabolic Requirements of Cell Proliferation. Annu. Rev. Cell Dev. Biol 27, 441–464 (2011). [PubMed: 21985671]
16. Otero YF, Stafford JM & McGuinness OP Pathway-selective insulin resistance and metabolic disease: the importance of nutrient flux. J. Biol. Chem 289, 20462–9 (2014). [PubMed: 24907277]
17. Uyeda K & Repa JJ Carbohydrate response element binding protein, ChREBP, a transcription factor coupling hepatic glucose utilization and lipid synthesis. Cell Metabolism 4, 107–110 (2006). [PubMed: 16890538]
18. Freudiger CW et al. Label-free biomedical imaging with high sensitivity by stimulated Raman scattering microscopy. Science (80-.). 322, 1857–61 (2008).
19. Min W, Freudiger CW, Lu S & Xie XS Coherent nonlinear optical imaging: beyond fluorescence microscopy. Annu. Rev. Phys. Chem 62, 507–530 (2011). [PubMed: 21453061]
20. Chung C-Y & Potma EO Biomolecular imaging with coherent nonlinear vibrational microscopy. Annu. Rev. Phys. Chem 64, 77–99 (2013). [PubMed: 23245525]
21. Cheng J-X & Xie XS Vibrational spectroscopic imaging of living systems: An emerging platform for biology and medicine. Science (80-.). 350, aaa8870–aaa8870 (2015).

22. Zhao Z, Shen Y, Hu F & Min W Applications of vibrational tags in biological imaging by Raman microscopy. Analyst (2017). doi:10.1039/C7AN01001J
23. Wei L et al. Live-cell bioorthogonal chemical imaging: stimulated Raman scattering microscopy of vibrational probes. Acc. Chem. Res 49, 1494–1502 (2016). [PubMed: 27486796]
24. Li M, Huang WE, Gibson CM, Fowler PW & Jousset A Stable isotope probing and Raman spectroscopy for monitoring carbon flow in a food chain and revealing metabolic pathway. Anal. Chem 85, 1642–9 (2013). [PubMed: 23259452]
25. Li J & Cheng J-X Direct Visualization of De novo Lipogenesis in Single Living Cells. Sci. Rep 4, 6807 (2015).
26. Long R et al. Two-color Vibrational Imaging of Glucose Metabolism by Stimulated Raman Scattering. Chem. Commun (2017). doi:10.1039/C7CC08217G
27. Sun RC et al. Noninvasive liquid diet delivery of stable isotopes into mouse models for deep metabolic network tracing. Nat. Commun (2017). doi:10.1038/s41467-017-01518-z
28. Longhi G, Zerbi G, Paterlini G, Ricard L & Abbate S Conformational dependence of CH(CD)-strechings in D-glucose and some deuterated derivatives as revealed by infrared and raman spectroscopy. Carbohydr. Res 161, 1–22 (1987).
29. Orringer DA et al. Rapid intraoperative histology of unprocessed surgical specimens via fibre-laser-based stimulated Raman scattering microscopy. Nat. Biomed. Eng 1, (2017).
30. Jung Y, Tam J, Jalian HR, Anderson RR & Evans CL Longitudinal, 3D In Vivo Imaging of Sebaceous Glands by Coherent Anti-Stokes Raman Scattering Microscopy: Normal Function and Response to Cryotherapy. J. Invest. Dermatol 1–6 (2014). doi:10.1038/jid.2014.293
31. Yoshikawa F et al. Opalin, a transmembrane sialylglycoprotein located in the central nervous system myelin paranodal loop membrane. J. Biol. Chem 283, 20830–20840 (2008). [PubMed: 18490449]
32. Bercury KK & Macklin WB Dynamics and mechanisms of CNS myelination. Developmental Cell 32, 447–458 (2015). [PubMed: 25710531]
33. Jurevics H & Morell P Cholesterol for Synthesis of Myelin Is Made Locally, Not Imported into Brain. J. Neurochem 64, 895–901 (1995). [PubMed: 7830084]
34. Cannon B & Nedergaard J Brown adipose tissue: function and physiological significance. Physiol. Rev 84, 277–359 (2004). [PubMed: 14715917]
35. Brehar FM et al. The development of xenograft glioblastoma implants in nude mice brain. J. Med. Life 1, 275–286 (2008). [PubMed: 20108505]
36. Flores CA, Hing SA, Wells MA & Koldovsky O Rates of triolein absorption in suckling and adult rats. Am. J. Physiol. Liver Physiol 257, G823–G829 (1989).
37. Lindquist S & Hernell O Lipid digestion and absorption in early life: An update. Current Opinion in Clinical Nutrition and Metabolic Care 13, 314–320 (2010). [PubMed: 20179589]
38. Pácha J Development of intestinal transport function in mammals. Physiol. Rev 80, 1633–67 (2000). [PubMed: 11015621]
39. Alberts B et al. Molecular Biology of the Cell. 4th *Edition,* New York (2002). doi:10.1091/mbc.E14-10-1437
40. Gaietta G et al. Multicolor and electron microscopic imaging of connexin trafficking. Science (80-.). 296, 503–507 (2002).
41. Dieterich DC et al. In situ visualization and dynamics of newly synthesized proteins in rat hippocampal neurons. Nat. Neurosci 13, 897–905 (2010). [PubMed: 20543841]
42. Wei L et al. Imaging Complex Protein Metabolism in Live Organisms by Stimulated Raman Scattering Microscopy with Isotope Labeling. ACS Chem. Biol 10, 901–908 (2015). [PubMed: 25560305]
43. Lewis CA et al. Tracing Compartmentalized NADPH Metabolism in the Cytosol and Mitochondria of Mammalian Cells. Mol. Cell 55, 253–263 (2014). [PubMed: 24882210]
44. Liu L et al. Malic enzyme tracers reveal hypoxia-induced switch in adipocyte NADPH pathway usage. Nat. Chem. Biol 12, 345–352 (2016). [PubMed: 26999781]
45. Kudryavtseva MV, Sakuta GA, Stein GI & Kudryavtsev b. N. The metabolic zonation of glycogen synthesis in rat liver after fasting and refeeding. Tissue Cell 24, 31–35 (1992). [PubMed: 1561624]

46. Jungermann K & Katz N Functional specialization of different hepatocyte populations. Physiol. Rev 69, 708–64 (1989). [PubMed: 2664826]
47. Fu D et al. In vivo metabolic fingerprinting of neutral lipids with hyperspectral stimulated Raman scattering microscopy. J. Am. Chem. Soc 136, 8820–8 (2014). [PubMed: 24869754]
48. Zhang L & Min W Bioorthogonal chemical imaging of metabolic changes during epithelial-mesenchymal transition of cancer cells by stimulated Raman scattering microscopy. J. Biomed. Opt 22, 1–7 (2017).
49. Hou J, Williams J, Botvinick E, Potma E & Tromberg BJ Visualization of breast cancer metabolism using multimodal non-linear optical microscopy of cellular lipids and redox state. Cancer Res. (2018).
50. Hong W et al. Antibiotic Susceptibility Determination within One Cell Cycle at Single-Bacterium Level by Stimulated Raman Metabolic Imaging. Anal. Chem (2018). doi:10.1021/acs.analchem.7b03382
51. Saar BG et al. Video-rate molecular imaging in vivo with stimulated Raman scattering. Science 330, 1368–1370 (2010). [PubMed: 21127249]
52. Saar BG, Johnston RS, Freudiger CW, Xie XS & Seibel EJ Coherent Raman scanning fiber endoscopy. Opt. Lett 36, 2396 (2011). [PubMed: 21725423]
53. Shen Y, Xu F, Wei L, Hu F & Min W Live-cell quantitative imaging of proteome degradation by stimulated Raman scattering. Angew. Chem. Int. Ed. Engl 53, 5596–9 (2014). [PubMed: 24737659]
54. Wei L et al. Live-cell imaging of alkyne-tagged small biomolecules by stimulated Raman scattering. Nat. Methods 11, 410–2 (2014). [PubMed: 24584195]
55. Lu F-K et al. Label-free DNA imaging in vivo with stimulated Raman scattering microscopy. Proc. Natl. Acad. Sci 112, 11624–11629 (2015). [PubMed: 26324899]

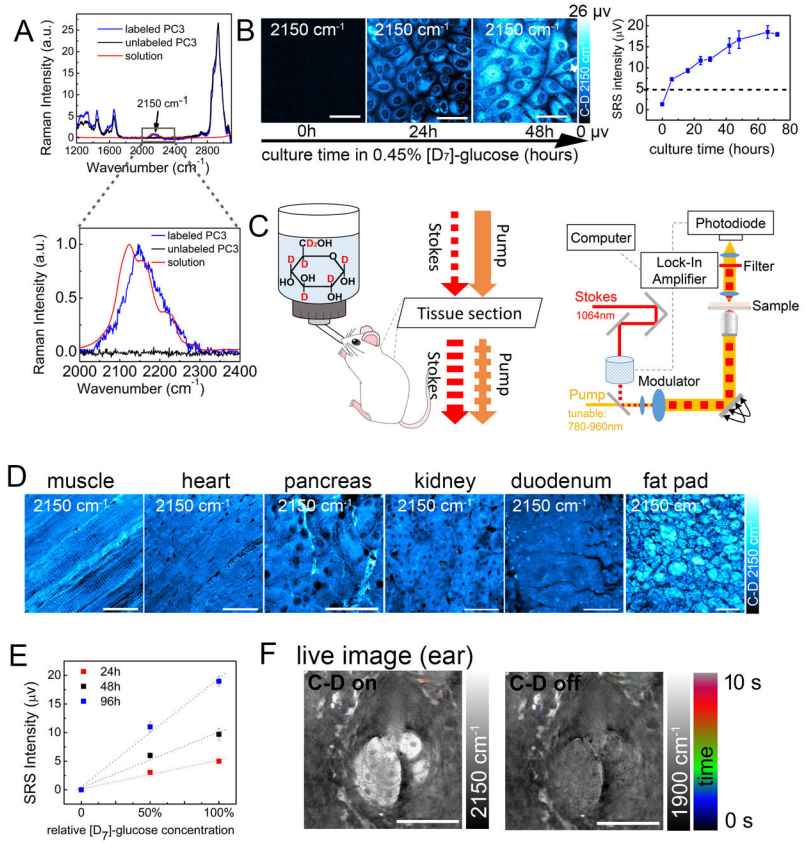

Fig. 1 l. SRS imaging of overall metabolic activity by [D_7]-glucose labeling.

a, Raman spectra normalized to C-D peak intensity, showing [D_7]-glucose solution (red), non-labeled PC3 cell (black), and PC3 cell labeled with 0.45% [D_7]-glucose for 72 hours (blue). Cell-silent region is magnified in the bottom. **b**, SRS imaging (at 2150cm^{-1}) of C-D label incorporation in PC3 cells labeled with 0.45% [D_7]-glucose for 0, 24, 48 hours. Time-dependent SRS intensity is quantified according to the images. Dashed line indicate estimated signal from intracellular glucose (~ 10mM12). Error bars, standard error (s.e.); n = 30. **c**, Illustration of experimental procedure. Mice were given [D_7]-glucose in the drinking water. Post mortem tissue was sectioned and imaged by SRS microscopy composing tunable near-IR pulsed lasers and laser-scanning microscopy. A high-frequency modulation transfer scheme is used to extract SRS signal from transmitted light. **d**, SRS imaging (at 2150cm^{-1}) of C-D label incorporation in several tissues from a mouse (P30) after drinking 10% [D_7]-glucose or water for 10 days. **e**, SRS intensity quantified from mice ear after labeling with 10% glucose, of which 0,50, or 100% is [D_7]-glucose, and the rest is unlabeled glucose. Three labeling duration (24, 48, 96 hr) were tested. Error bars, s.e.; n = 4. **f**, SRS images of a living mouse ear skin that has been administered 5% [D_7]-glucose in drinking water for 8 days, showing temporal color-coded on-resonance signal (2150cm^{-1}) and off-resonance background (1900cm^{-1}) channels acquired at speed of 1.6 sec per frame. Scale bars, 50μm.

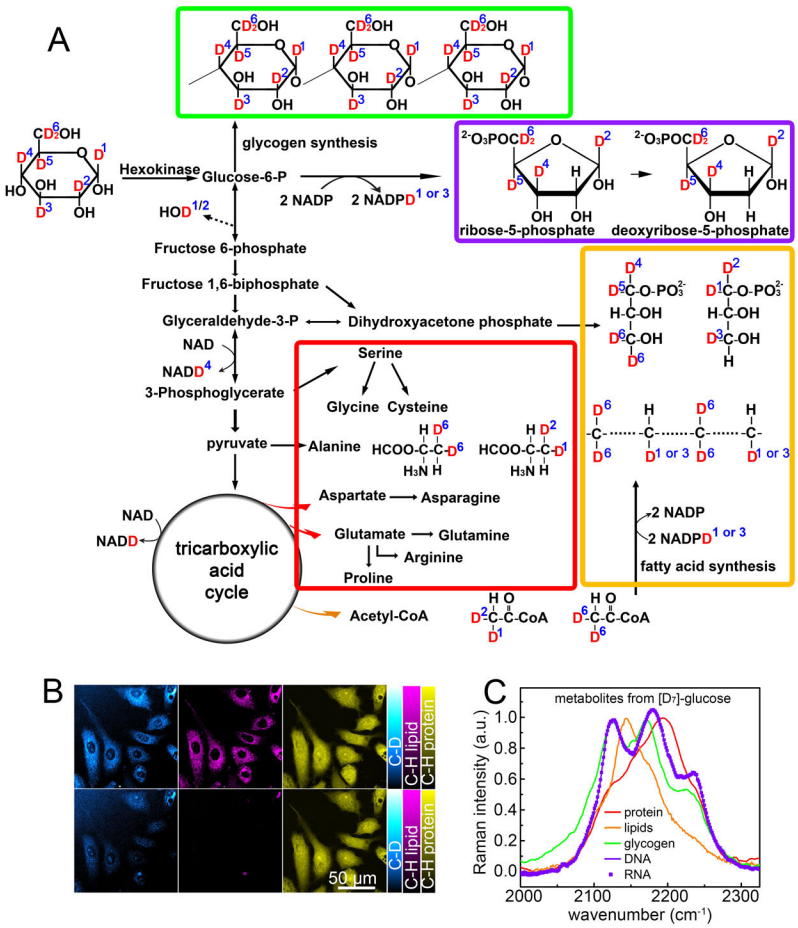

Fig. 2 |. Principle of Spectral TRacIng of DEuterium isotope (STRIDE).

a, Deuterium transfer traced along major biosynthetic pathways derived from [D_7]-glucose. **b**, PC3 cells labeled with 0.45% [D_7]-glucose for 48hrs, before (upper) and after (bottom) methanol wash for 10min. Images were also shown for unlabeled lipid (magenta) and protein (yellow) channel in the C-H frequencies. **c**, Normalized C-D Raman spectra of four glucose-derived macromolecule metabolites, including glycogen from [D_7]-glucose-fed mouse liver (fasted overnight and acutely stimulated and labeled by 10% [D_7]-glucose for 8 hours), and protein, lipids or nucleic acids (including DNA and RNA) extracted from HeLa cells cultured with 0.45% [D_7]-glucose for 6 days.

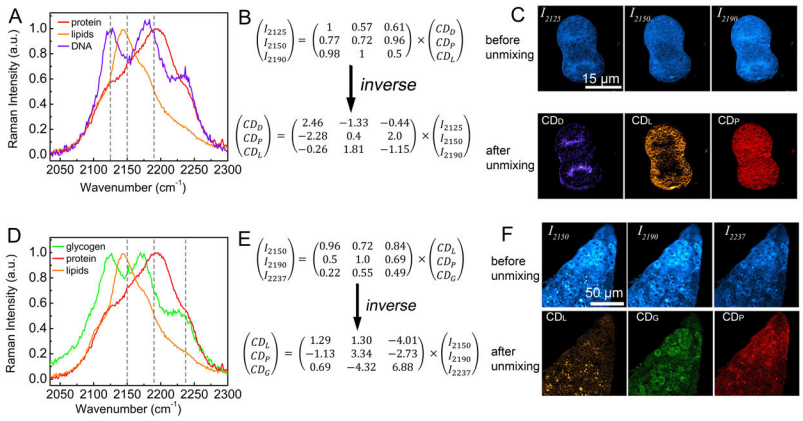

Fig. 3 | Multiplexed imaging of macromolecule biosynthesis activity using STRIDE of [D_7]-glucose.

a, Raman spectra of [D_7]-glucose-derived proteins, lipids, and DNA, as in Fig. 2c. Dashed lines indicate imaging frequencies for corresponding macromolecules. **b**, Linear unmixing algorithm for proteins, lipids, and DNA. I_X, image intensity for corresponding frequencies. CD_X, calculated intensity for corresponding macromolecules. **c**, Images of a [D_7]-glucose-labeled mitotic HeLa cell before and after unmixing. **e**, Raman spectra of [D_7]-glucose-derived proteins, lipids, and glycogen, as in Fig. 2c. Dashed lines indicate imaging frequencies for corresponding macromolecules. **f**, Linear unmixing algorithm for proteins, lipids, and glycogen. I_X, image intensity for corresponding frequencies. CD_X, calculated intensity for corresponding macromolecules. **g**, Images of a [D_7]-glucose-fed mouse liver before and after unmixing.

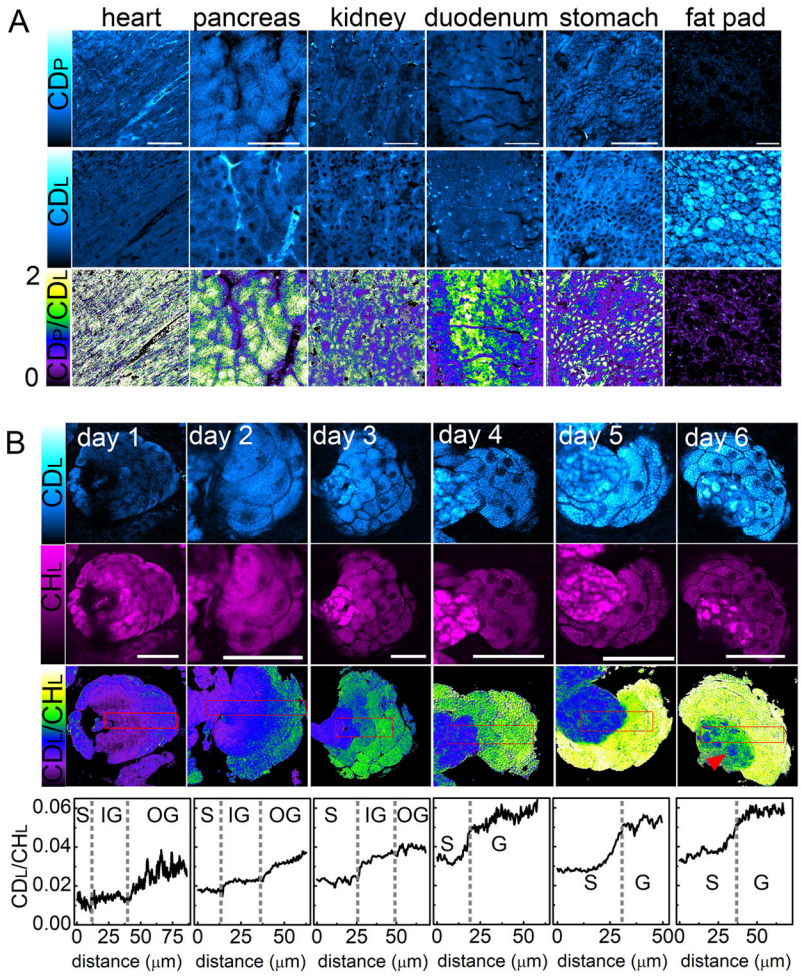

Fig. 4 |. STRIDE imaging in mouse tissue

a, Unmixed CD_L and CD_P images of various tissue slices from mouse (P30) after drinking 10% [D_7]-glucose for 10 days. Ratiometric images were calculated as CD_P/CD_L to represent functional divergence of glucose utilization. **b**, Time-dependent tracking of CD_L and CH_L images of the sebaceous gland from a mouse drinking 5% [D_7]-glucose water for 1-6 days. Ratiometric images were calculated as CD_L/CH_L to represent lipid turnover dynamics. Arrows indicate remnants of sebocytes. Line profiles were plotted below for the boxed area. Dashed lines indicate boundaries identified by morphology. S, sebum; IG, inner gland; OG, outer gland; G, gland. Scale Bars, 50μm.

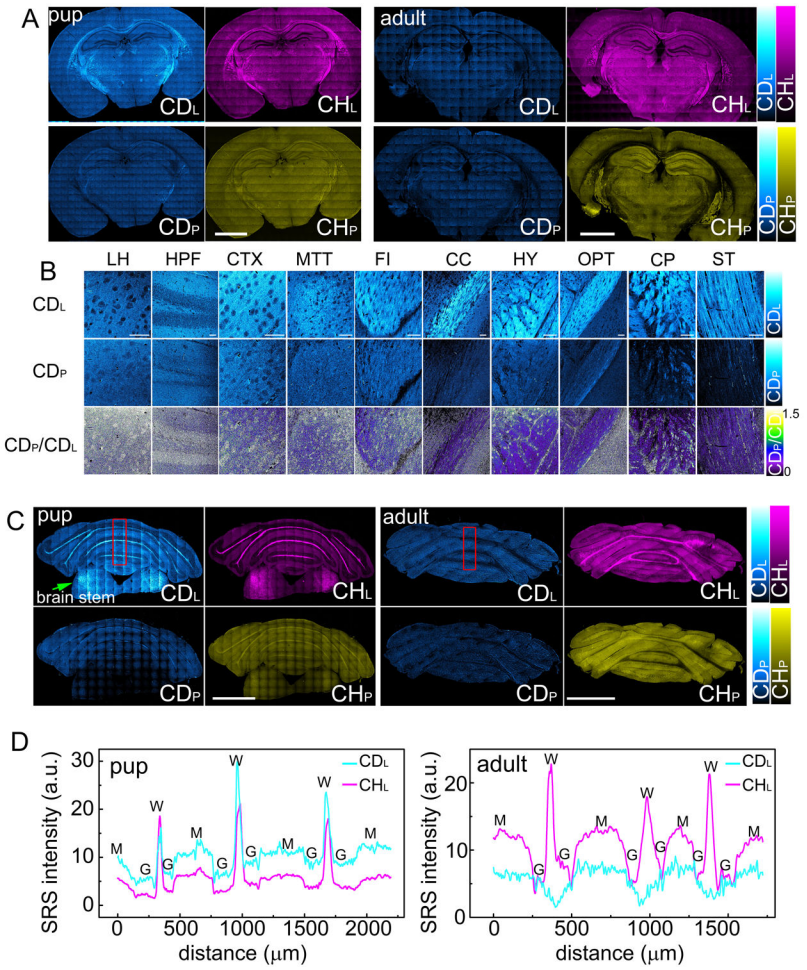

Fig. 5 |. STRIDE imaging of protein and lipid biosynthesis in mouse brain.

a, Imaging lipid (CD_L) and protein (CD_P) synthesis in cerebrum of pup (P21) and adult mice (P100). Pup mouse was labeled with 2% [D_7]-glucose during the developmental period (E11 to P21) through the drinking water of its mother. Adult mouse was labeled with 2% [D_7]-glucose for 30 days. Unlabeled lipid (CH_L) and protein (CH_P) are also shown. **b**, Magnified images from different areas in (**a**). Ratiometric images were calculated as CD_P/CD_L. **c**, Imaging lipid (CD_L) synthesis in cerebellum of same pup and adult mice as in (**a**). **d**, Line profiles of lipid synthesis (CD_L) and unlabeled lipid (CH_L) shown for the boxed area in (**c**). M, molecular layer; G, granule cell layer; W, white matter. Scale Bars, 2mm in (**a**,**c**) and 50μm in (**b**).

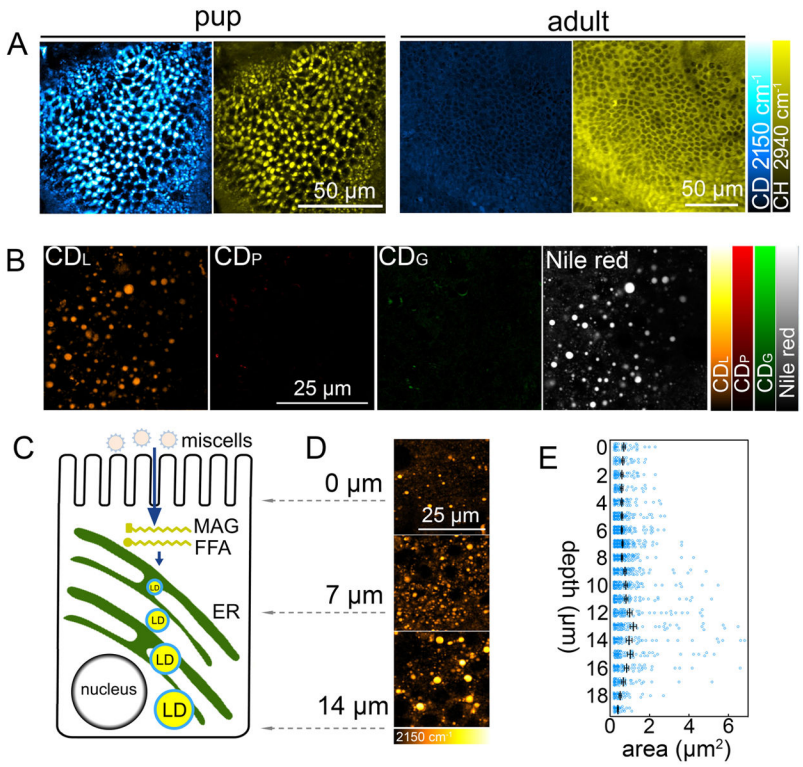

Fig. 6 |. STRIDE imaging reveals fast and unidirectional lipid absorption in newborn mouse intestine

a, Images of intestinal epithelium (duodenum) from the same pup and adult as in Fig. 4a. CD and CH images represent glucose-derived signal and unlabeled biomass signal, respectively. **b**, Images of intestinal epithelium (duodenum) from a pup (P10) after 15min feeding with milk from a lactating mouse administered 10% [D_7]-glucose for 5 hours. Images show separation of glucose-derived CD signal into lipid (CD_L), protein (CD_P), glycogen (CD_G) channels, and correlative Nile Red confocal fluorescence of the stained tissue. **c**, Illustration of fat absorption across the enterocyte of intestinal epithelium. MAG, monoacylglyceride; FFA, free fatty acid; LD, lipid droplet; ER, endoplasmic reticulum. **d**, Images of glucose-derived lipid synthesis acquired at different depth across the intestinal enterocyte. **e**, Quantitative analysis of depth profile of LD size distribution. Data are presented as scattered plots of individual LDs and their mean ± s.e.

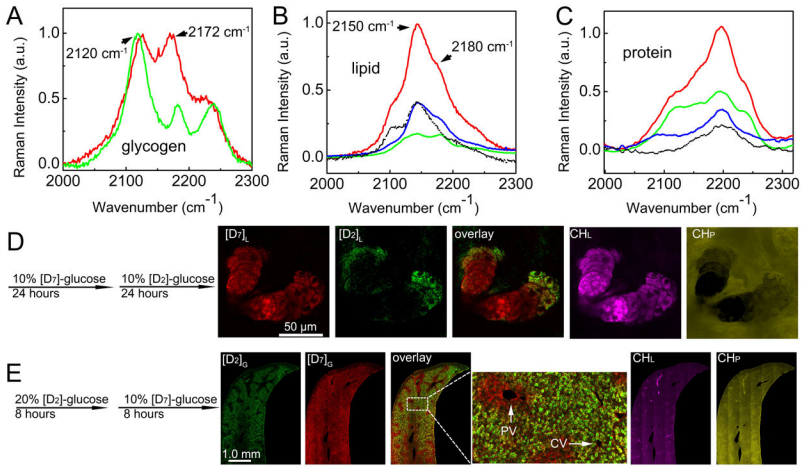

Fig. 7 |. Pulse-chase STRIDE imaging of metabolic dynamics through sequentially labeled [D_7]- and [D_2]- glucose

a, C-D Raman spectra of liver glycogen derived from [D_7]- or [6,6-D_2]-glucose-fed mice. Overnight-fasted mice were stimulated and labeled with 10% [D_7]-glucose or [6,6-D_2]-glucose for 8 hrs, and liver tissues were used for Raman spectra acquisition. Red, from [D_7]-glucose-fed mouse; green, from [6,6-D_2]-glucose-fed mouse. **b**, Raman spectra of lipid extracts from HeLa cells cultured with 0.45% [D_7]-, [6,6-D_2]-, or [1-D_1]-glucose for 6 days, and normalized at 1450cm^{-1} (lipid C-H bending). Red, from [D_7]-glucose-cultured cell; green, from [6,6-D_2]-glucose-cultured cell; blue, from [1-D_1]-glucose. Black dashed curve is calculated by subtracting the latter two signals from [D_7]-derived signal. **c**, Raman spectra of protein extracts from HeLa cells cultured with 0.45% [D_7]-, [6,6-D_2]-, or [1-D_1]-glucose for 6 days. Normalized at 1670cm^{-1} (protein Amide I band). Red, from [D_7]-glucose; green, from [6,6-D_2]-glucose, blue, from [1-D_1]-glucose. Black dashed curve is calculated by subtracting the latter two signals from [D_7]-derived signal. **d**, Unmixed images of lipid signal derived from 10% [D_7]-glucose ([D7]$_L$) and [6,6-D_2]-glucose ([D2]$_L$) labeling in successive 24-hr time windows in mouse. Images were taken from sebaceous gland of ear skin. Overlay of [D7]$_L$ and [D2]$_L$ channels show different spatial distribution. Unlabeled lipid (CH_L) and protein (CH_P) are also shown. **e**, Unmixed images of glycogen signal derived from 20% [D_2]-glucose ([D2]$_G$) and 10% [D_7]-glucose ([D7]$_G$) labeling in successive 8-hr time windows in overnight-fasted mouse. Images were taken from liver tissue slice. Overlay of [D2]$_G$ and [D7]$_G$ channels show different spatial distribution. Portal vein (PV) and central vein (CV) are discerned by the existence of triad structure.